Materials and Interfaces

Scilight

Article

AuCu-Based Solid-Hollow Hybrid Nanostructures for Efficient Photothermal Therapy against Multidrug-Resistant Bacteria

Qiuping Yang [1,†], Qian Wu [2,†], Xiaowen Chen [3,†], Xiaoying Shen [4,†], Yi Wang [2,*], Xiaohu Wu [5,*], Yanyun Ma [6], Pu Zhang [4,*], and Yiqun Zheng [1,*]

[1] School of Chemistry, Chemical Engineering and Materials, Jining University, Qufu 273155, China
[2] Chongqing Key Laboratory of Green Synthesis and Applications, College of Chemistry, Chongqing Normal University, Chongqing 401331, China
[3] College of Electromechanical Engineering, Qingdao University of Science and Technology, Qingdao 266061, China
[4] Chongqing Research Center for Pharmaceutical Engineering, College of Pharmacy, Chongqing Medical University, Chongqing 400016, China
[5] Yangtze Laboratory, Wuhan 430205, China
[6] Jiangsu Key Laboratory of Advanced Negative Carbon Technologies, Institute of Functional Nano & Soft Materials (FUNSOM), Soochow University, Suzhou 215123, China
* Correspondence: ywang@cqnu.edu.cn (Y.W.); wuxiaohu@pku.org.cn (X.W.); zhangpu@cqmu.edu.cn (P.Z.); yzheng@jnxy.edu.cn (Y.Z.)
† These authors contributed equally to this work.

Received: 10 August 2025; Revised: 3 September 2025; Accepted: 25 December 2025; Published: 30 December 2025

Abstract: Hybrid nanostructures incorporating anisotropic structural components present promising opportunities for developing advanced photothermal agents. Here, we report the controlled synthesis of solid–hollow hybrid nanostructures based on gold–copper (Au–Cu) and demonstrate their photothermal antibacterial properties. Starting from Au nanoplate seeds, we achieve anisotropic deposition to synthesize AuCu and AuAgCu Janus nanostructures. The newly-deposited regions are subsequently transformed into porous architectures via a galvanic replacement reaction mediated by KCl and acetic acid. The introduced nanopores enhance near-infrared (NIR) absorption, thereby improving photothermal conversion efficiency under both 808 nm and 1064 nm laser irradiation and enabling the efficient eradication of multidrug-resistant bacteria. Finite-difference time-domain (FDTD) simulations confirm their optimized plasmonic properties. The current study underscores the potential of morphologically complex hybrid nanostructures for advanced photothermal applications.

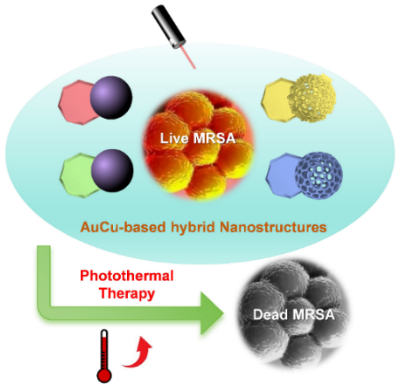

Keywords: hybrid; noble metal; two dimensional; porous; photothermal conversion; FDTD simulation

1. Introduction

Hybrid nanostructures have attracted considerable research interest owing to their unique asymmetric architectures and broad applicability in fields such as catalysis, biomedicine, energy storage, and environmental remediation [1–3]. These structures are defined by their integration of distinct material domains or morphological features within a single entity, enabling multifunctionality through compartmentalized or spatially varied properties [4]. In plasmonics, which exploits localized surface plasmon resonance (LSPR) to confine and enhance electromagnetic (EM) fields, hybrid nanostructures provide a versatile platform for tailoring optical responses beyond the limits of symmetric counterparts [5,6]. Their inherent structural or compositional asymmetry facilitates a non-uniform distribution of plasmonic fields, generating localized hotspots at designated regions [7,8]. This capability becomes especially valuable when structural features of varied morphologies—such as two-dimensional (2D) plates and zero-dimensional (0D) spheres—are integrated into one hybrid entity, enhancing their utility in applications like photothermal therapy and high-sensitivity optical sensing [9–12].

Previous research on hybrid nanostructures has largely emphasized compositional heterogeneity, combining materials such as metals, semiconductors, and polymers [13–15]. Recent advances have expanded the scope, shifting from compositional heterogeneity toward the integration of components with distinct morphological features. This focus on structural hybridity opens new avenues to modulate plasmonic behavior, enhance light–matter interaction, and introduce directional functionality [10,16–20].

However, integrating diverse morphological features into a single nanoentity remains synthetically challenging, primarily due to the competing growth kinetics and thermodynamic preferences involved in forming distinct architectures within one structure [21,22]. While conventional one-pot syntheses often lack the precision to simultaneously regulate these multiple structural parameters, the seeded growth approach offers a more controlled pathway [23,24]. This method enables site-specific deposition on preformed seeds, typically through symmetry breaking of face-centered cubic (*fcc*) metals combined with region-specific capping or kinetic modulation [25–28]. Furthermore, the synthetic strategy can be extended by post-synthetic modifications such as oxidative etching [29,30], which allows the solid domains readily converted into hollow ones, thereby introducing porosity, increasing surface area, and creating complex hybrid nanoentities [31].

Herein, we report the synthesis of gold-copper (AuCu)-based solid-hollow hybrid nanostructures that were achieved through controlled seeded growth followed by galvanic replacement. These nanostructures are subsequently applied to the photothermal eradication of multidrug-resistant bacteria. Our synthesis begins with the formation of plate-like Au nanoparticles as seeds, followed by the anisotropic deposition of Cu or CuAg to anchor quasi-spherical particles onto the plate seeds, yielding AuCu or AuAgCu Janus nanostructures, respectively. Subsequent treatment with an Au precursor ($HAuCl_4$) in a KCl/acetic acid (HAc) solution tempers and spatially confines the galvanic replacement reaction. This process preferentially oxidizes the newly deposited domains into porous, hollow architectures, while concurrently reducing Au^{3+} ions for deposition.

Compared to previous reports on AuCu-based systems, our methodology advances the field in several key aspects: (i) it achieves the hybrid integration of divergent morphological features, combining solid 2D plates with solid/hollow 0D quasi-spheres into single architectures; (ii) the use of KCl/HAc mildens the galvanic replacement process, allowing it to proceed in a controlled manner that is confined to the newly-deposited quasi-spherical domain while largely preserving the solid plate; and (iii) The introduction of Ag to the galvanic replacement reaction acts as a modulator, reducing the dimensions of the resulting nanopores within the hollow domain. These solid–hollow hybrid nanostructures exhibit satisfactory photothermal conversion efficiency and antibacterial properties due to their engineered asymmetry and porous morphology.

2. Experimental Details

2.1. Materials

Gold(III) chloride trihydrate ($HAuCl_4·3H_2O$, 99.9%), copper(II) nitrate trihydrate ($Cu(NO_3)_2·3H_2O$, 99%), ascorbic acid (AA, 99.0%), and hexadecyltrimethylammonium bromide (CTAB, 99%) were sourced from Aladdin Chemical (Shanghai, China) and utilized without further purification. Silver nitrate ($AgNO_3$, analytical grade), potassium chloride (KCl, analytical grade), and hexamethylenetetramine (HMTA, ≥98.0%) were all purchased from Sinopharm Group in Shanghai, China. Acetic acid (HAc, 99.8%) was obtained from Tianjin Fuyu Fine Chemical Co., Ltd. (Tianjin, China). Octadecyltrimethylammonium chloride (OTAC, 90%) was acquired from Lvsen Chemical (Linyi, China). For all experiments, deionized water with a resistivity of 18.2 MΩ·cm was employed, which was generated by an ultrapure water system from Ulupure (Beijing, China).

2.2. Synthesis of Au Nanoplates (Au NPs)

An aqueous solution of Au NPs was prepared according to the method described in our previous study [32]. It began with the combination of 5 mL of OTAC (10 mM) and 6 mL of $HAuCl_4$ (0.5 mM) at room temperature. The mixture was cooled in an ice-water bath for 10 min. Following this, 1 mL of ascorbic acid (AA, 10 mM) was added, inducing an immediate color change to light green. The solution was then allowed to age at ice-water bath for 30 min before use.

2.3. Synthesis of AuCu and AuAgCu Janus Nanostructures (JNSs)

For the synthesis of AuCu JNSs, 1.4 mL of CTAB (200 mM) was added to the aqueous Au NP suspension. Subsequently, 100 mg of solid AA was introduced, followed by the sequential addition of 1 mL of HMTA (100 mg mL^{-1}) and 0.1 mL of $Cu(NO_3)_2$ (50 mg mL^{-1}) solution. The mixture was homogenized by ultrasonication and then aged in an oil bath at 80 °C for 3 h. the protocol remained identical except for the introduction of an $AgNO_3$ solution (2 mM, 0.625 mL) alongside the Cu precursor.

2.4. Synthesis of AuCu and AuAgCu Porous Hybrid Nanostructures (PHNSs)

The synthesis of AuCu PHNSs was initiated by adding 0.1 mL of KCl (30 mg mL^{-1}) to the aqueous suspension of as-prepared AuCu JNSs. Subsequently, 0.2 mL of acetic acid and 0.1 mL of $HAuCl_4$ (20 mM) were introduced. The mixture was dispersed uniformly via ultrasonication and then reacted under stirring at room temperature for 2 h. The procedure for AuAgCu PHNSs was identical, with the sole modification being the use of AuAgCu JNSs as the starting material.

2.5. Instruments

Transmission electron microscopy (TEM) images were captured using a HT7820 microscope (Hitachi, Tokyo, Japan) operated at 120 kV accelerating voltage. High-resolution TEM (HRTEM), selected-area electron diffraction (SAED), high angle annular dark field-scanning transmission electron microscopy (HAADF-STEM) and energy-dispersive X-ray STEM (EDX-STEM) mapping were performed using a Talos F200X (FEI, Hillsboro, OR, USA) microscope operated at 200 kV accelerating voltage. The crystalline structures were analyzed with a MiniFlex600 X-ray diffractometer (XRD, Rigaku Corporation, Tokyo, Japan). X-ray photoelectron spectroscopy (XPS) measurements were performed using a Thermo Fisher Scientific KALPHA XPS (Thermo Fisher Scientific Inc., Waltham, MA, USA) with monochromatic Al K_α radiation ($h\nu = 1486.6$ eV). Extinction spectra were recorded using a UV2310II dual-beam UV-vis-NIR spectrometer (Techcomp Ltd., Shanghai, China). The thermal image was taken by FOTRIC 220s infrared thermal imager (JIUHENG, Shanghai, China). The 808 nm and 1064 nm lasers used in the experiments were models DS3-51512-K808DAHRN-10.00W and DS3-51512-K1064HAMRA-10.00W, respectively, supplied by BWT (Beijing, China).

2.6. Photothermal Measurement

The photothermal effect of the as-prepared products was measured using a laser (wavelength: 808 nm or 1064 nm) and an infrared thermal imager. Typically, the as-prepared products were purified, resuspended in water, and 1.7 mL of the resulting suspension was added to each well of a 48-well plate. The aqueous suspensions were completely covered by adjusting the size of the laser spot, followed by the irradiation under the laser (1 $W{\cdot}cm^{-2}$) for 10 min. Throughout the measurement, the solution temperature was monitored using an infrared thermal imager, data was recorded at the set interval of 10 s, and the *T*-*t* curve was simultaneously mapped.

2.7. Calculation of the Photothermal Conversion Efficiency

The photothermal conversion efficiency (η) was calculated according to the following formula proposed by Roper [33],

$$\eta = \frac{hA(\Delta T_{\max} - \Delta T_{\mathrm{H_2O}})}{I(1 - 10^{-A_\lambda})}$$

where h is the heat transfer coefficient, A is the surface area for radiative heat transfer, $\Delta T_{\max}$ represents the maximum steady-state temperature in the presence of products relative to room temperature, $\Delta T_{\mathrm{H_2O}}$ represents the maximum steady state temperature of water relative to room temperature, I is the power density of used laser, and A_λ is the absorbance of products at 808 or 1064 nm.

2.8. *FDTD Simulation*

Based on the Finite Element Method (FEM), the photothermal conversion characteristics were calculated. The refractive index of the material determines the optical properties of the nanoparticles, and the complex refractive indices of Au, Ag, and Cu used in the calculation were taken from previous studies [34]. Here, the real part, *n*, determines the propagation speed of light waves in the medium, while the imaginary part, *k*, represents the absorption performance of the medium for electromagnetic waves. The medium surrounding the nanoparticles is water, with a refractive index of 1.33. The incident light intensity was set to 10^9 W m^{-2} [35]. The spherical region outside the nanoparticles was set as a perfect matching layer (PML) to reduce the influence of boundary reflections.

3. Results and Discussion

3.1. Synthesis and Characterizations of AuCu-Based Hybrid Nanostructures

The synthesis proceeded in three steps, as outlined in Scheme 1. First, plate-like Au seeds were prepared according to our previous study (Figure S1) [36]. Next, Cu or CuAg atoms were deposited by reducing their precursors in the presence of CTAB, AA, and HMTA [37]. As shown in Figure S2, quasi-spherical particles formed asymmetrically on one side of the Au plates in both cases, with the underlying plate remaining visible—consistent with the formation of Janus nanostructures (JNSs). EDX-STEM mapping of the products revealed distinct compositional profiles. For Cu-only deposition, Cu localized predominantly on the quasi-spherical particles, leaving the plate region Au-rich (Figure S3). In contrast, co-deposition of Cu and Ag resulted in Cu-enriched quasi-spherical particles, whereas the plate region contained both Au and Ag (Figure S4). This suggests that Ag readily alloys with Au, likely due to their close lattice matching, whereas the significant Au/Cu lattice mismatch promotes heterogeneous Cu deposition. Based on their composition, these two types of products are designated as AuCu JNSs and AuAgCu JNSs, respectively.

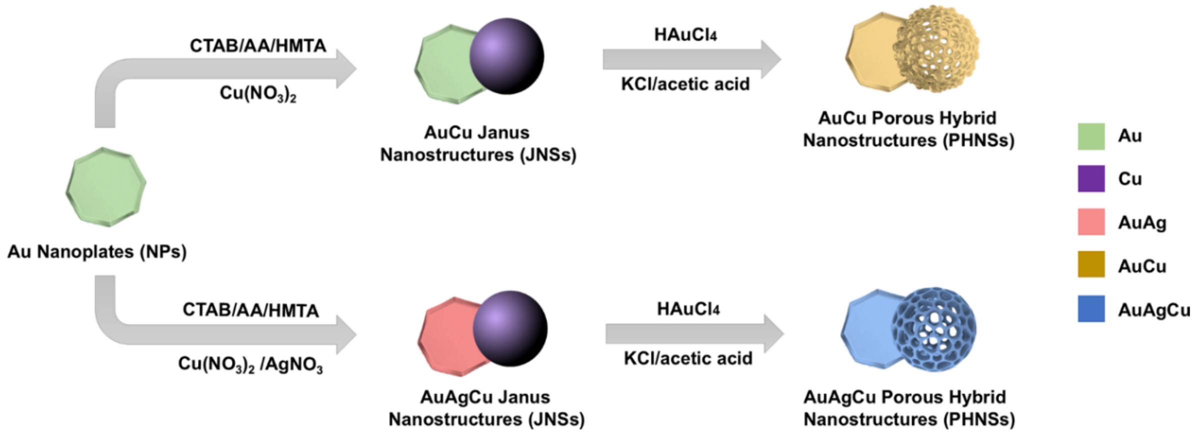

Scheme 1. Schematic illustration showing the formation process of AuCu-based hybrid nanostructures.

The third step involved a galvanic replacement reaction, where AuCu JNSs and AuAgCu JNSs were reacted with $HAuCl_4$ in the presence of KCl and acetic acid. For both cases, the quasi-spherical component transformed into a porous structure while the plate-like seeds were retained, as confirmed by TEM (Figures 1a–c and 2a–c) and HAADF-STEM images (Figures 1f and 2f). For the product derived from AuCu JNSs, lattice fringes of the solid and hollow regions measured 0.23 nm (Figure 1d) and 0.20 nm (Figure 1e), corresponding to the (111) planes of Au and a Cu/Au alloy, respectively. For the products from AuAgCu JNSs, the hollow and solid regions exhibited lattice fringes of 0.21 nm (Figure 2d) and 0.22 nm (Figure 2e), corresponding to the (111) planes of a Cu/Ag/Au alloy and Au, respectively. For both types of products, EDX-STEM elemental mapping images (Figures 1g–i and 2g–j, Figure S5a,b) demonstrated a roughly homogeneous distribution of the constituent metals. The distinct lattice spacings, however, indicate the formation of local compositional gradients, resulting in regions with Au-rich and alloy-dominated crystalline phases. This redistribution and phase evolution are attributed to the etching and in situ regrowth occurring during the galvanic replacement reaction. Given their distinct structural features and compositions, the final products shown in Figures 1 and 2 are designated as AuCu porous hybrid nanostructures (PHNSs) and AuAgCu PHNSs, respectively.

Pore size analysis (Figure S6) revealed average diameters of 7.5 ± 3.9 nm for AuAgCu PHNSs and 58.8 ± 20.7 nm for AuCu PHNSs. This variation in pore size is attributed to the dual galvanic replacement reactions enabled by the participation of Ag. When Cu and Ag are both present, their differing standard reduction potentials and reaction kinetics with $AuCl_4^-$ result in a competitive yet synergistic process of etching and redeposition. This complex in situ regrowth, involving two sacrificial metals, governs the final scale of the porous architecture.

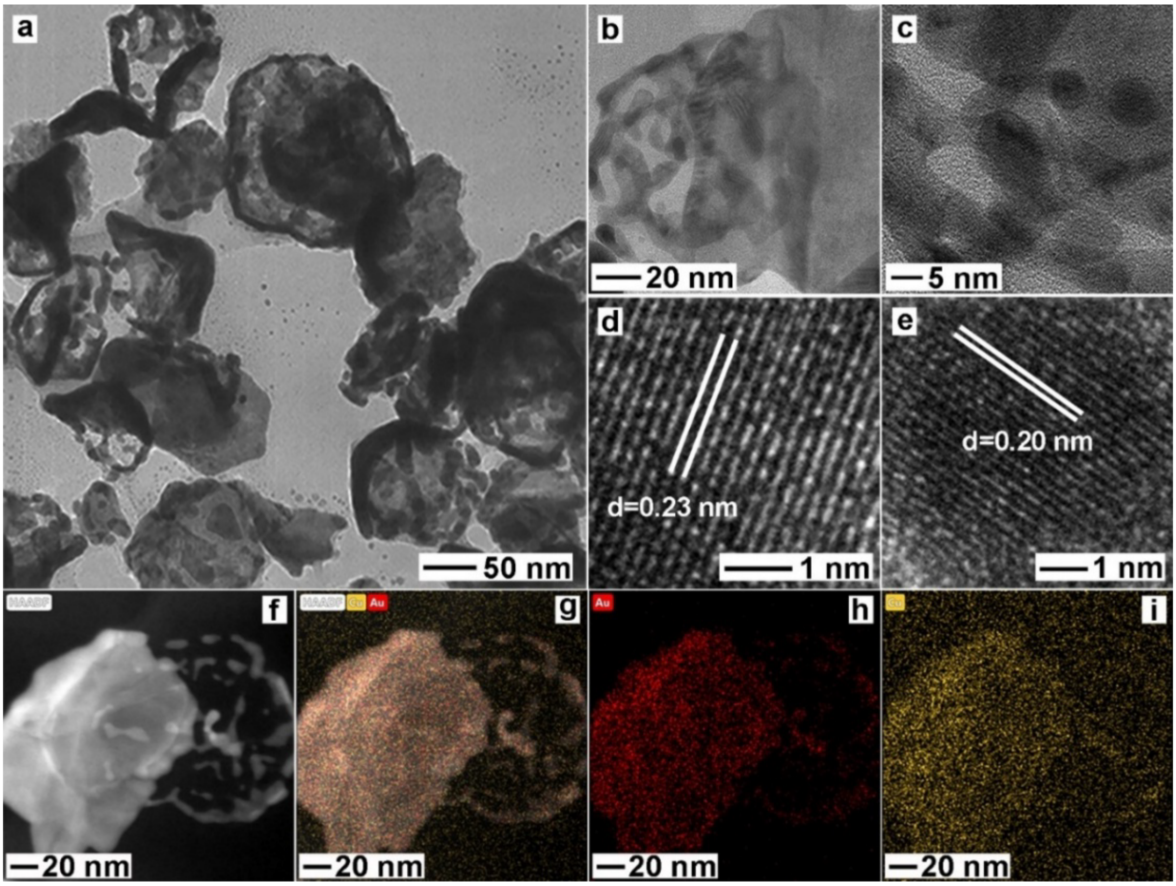

Figure 1. Morphology and structural characterizations of AuCu PHNSs: (**a**–**c**) TEM; (**d**,**e**) HRTEM; (**f**) HAADF-STEM; (**g**–**i**) EDX-STEM mapping; (**g**) HAADF + Cu + Au; (**h**) Au; and (**i**) Cu.

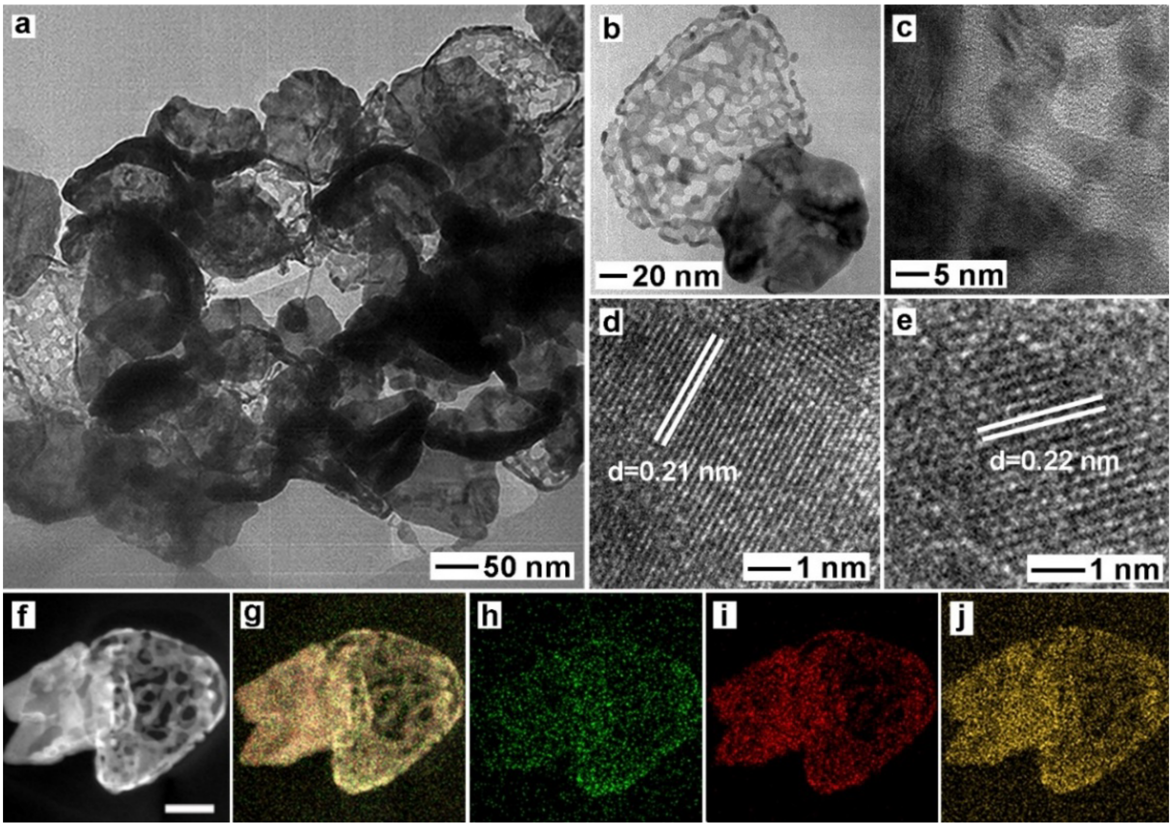

Figure 2. Morphology and structural characterizations of AuAgCu PHNSs: (**a**–**c**) TEM; (**d**,**e**) HRTEM; (**f**) HAADF-STEM; (**g**–**j**) EDX-STEM mapping; (**g**) HAADF + Cu + Ag + Au; (**h**) Ag; (**i**) Au; (**j**) Cu. The scale bar in (**f**) is 50 nm and applies to (**g**–**j**).

3.2. XRD and XPS Characterizations

To gain further insights into the structural properties, an array of characterizations was conducted. EDS measurements of four types of products were conducted. As shown in Figure S7, the Au/Cu atomic ratio of AuCu JNSs and AuCu PHNSs was 89.0:11.0 and 74.2:25.8, respectively. The atomic ratio of Au/Ag/Cu atomic ratio of AuAgCu JNSs and AuAgCu PHNSs was 82.4:14.2:3.3 and 66.8:23.4:9.8, respectively.

XRD measurements were conducted and the diffraction peaks observed for all products were compared with standard references for Au, Ag, and Cu, as shown in Figure 3. The results indicate good consistency with the face-centered cubic (*fcc*) structure of these metals. For the patterns of AuCu-based NSs, two distinct sets of diffraction peaks were observed, corresponding to *fcc*-Cu and *fcc*-Au/Ag, respectively (Table S1). X-ray photoelectron spectroscopy (XPS) measurements were performed to investigate the valence electronic states of elements in the four products. The Cu 2p spectra (Figure 4a–d) were deconvoluted into two components: the lower binding energy component at 931–932 eV was assigned to two possible valence states, Cu(I) or Cu(0), while the peaks at higher binding energies of 933–934 eV were attributed to $Cu(OH)_2$. The presence of weak satellite peaks in the binding energy range of 940 to 948 eV, corresponding to shake-up structures, further confirms the minimal presence of Cu(II) species. In the corresponding Cu LMM spectra (Figure 4e–h), the kinetic energy peaks centered at 915 eV were assigned to Cu(I) species. Since no Cu(I) species were detected in the XRD patterns, their presence is likely due to the oxidation of metallic nano-Cu under ambient conditions. The deconvolution of the doublets in the Au 4f spectra (Figure 4i–l) and Ag 3d spectrum (Figure S8) were performed. Specifically, the major presence of a doublet with the binding energy peaks located at around 88 eV (Au $4f_{5/2}$), 84 eV (Au $4f_{7/2}$), 374 eV (Ag $3d_{3/2}$), and 368 eV (Ag $3d_{5/2}$) confirmed the predominance of Au and Ag atoms in their zerovalent states. The slight shift in B.E. peak positions should be attributed to the electronic interactions among these metals. All the obtained data are summarized in Table S2.

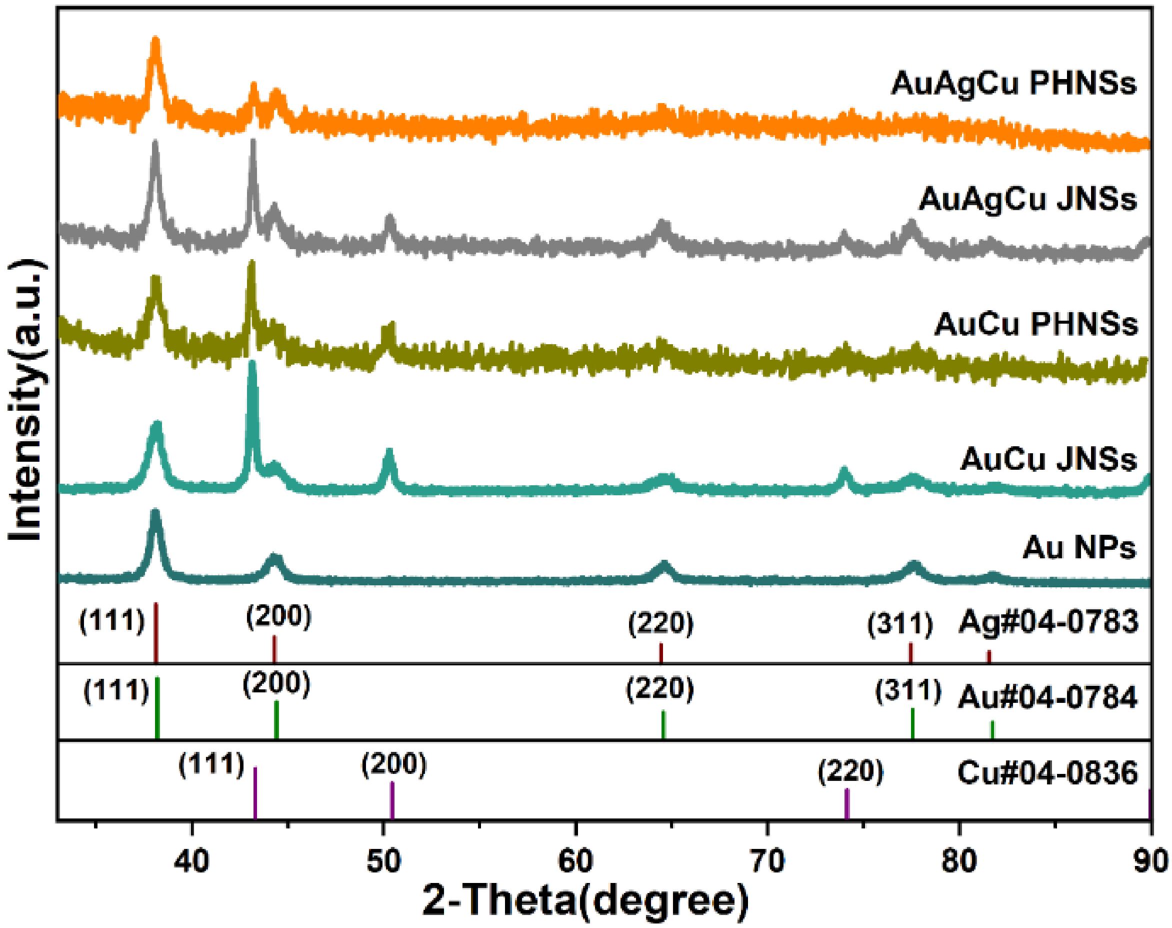

Figure 3. XRD patterns of AuCu JNSs, AuAgCu JNSs, AuCu PHNSs, and AuAgCu PHNSs. Reference peak positions for metallic Cu, Ag, and Au are indicated for comparison.

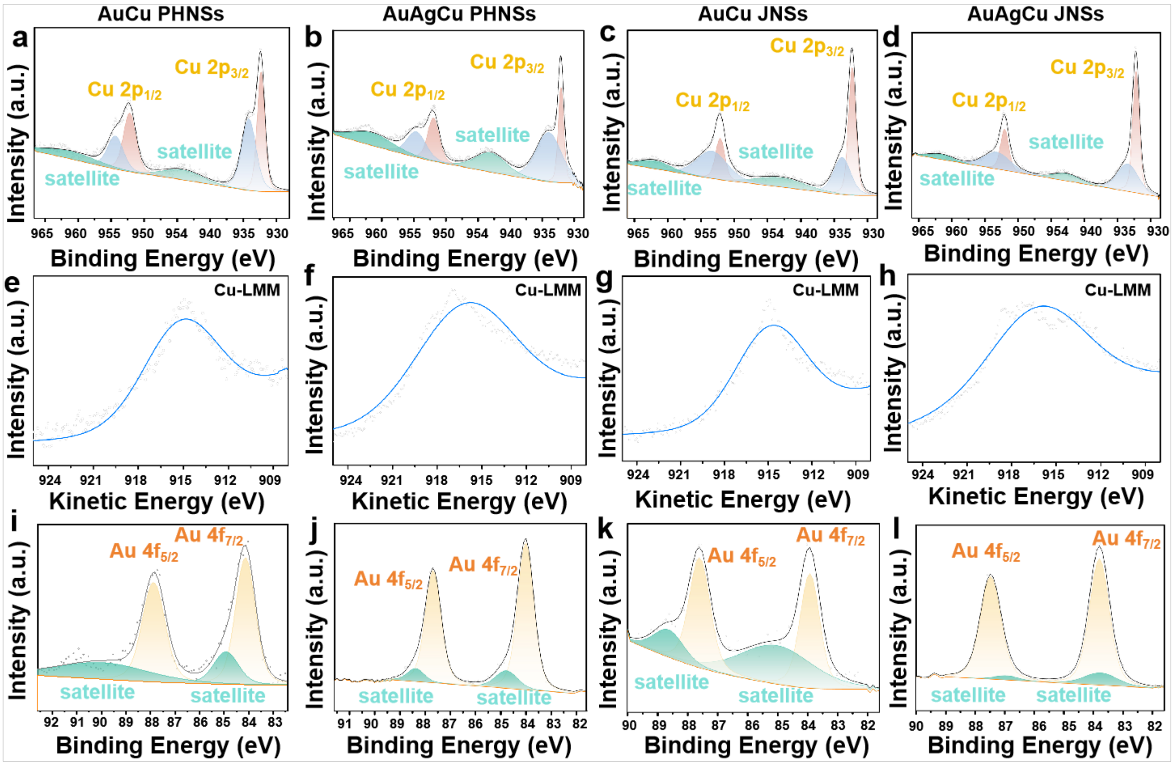

Figure 4. XPS spectra for (**a**–**d**) Cu 2p; (**e**–**h**) Cu LMM; and (**i**–**l**) Au 4f regions. From left to right, the columns correspond to (**a**,**e**,**i**) AuCu PHNSs; (**b**,**f**,**j**) AuAgCu PHNSs; (**c**,**g**,**k**) AuCu JNSs; and (**d**,**h**,**l**) AuAgCu JNSs.

3.3. Formation Mechanism

The selective etching of the quasi-spherical regions, while preserving the plate-like part, is fundamentally driven by electrochemical potential differences. Thermodynamically, the higher reduction potential of Au^{3+}/Au (+1.50 V vs. SHE) compared to Cu^{2+}/Cu (+0.34 V vs. SHE) and Ag^{+}/Ag (+0.80 V vs. SHE) drives the galvanic replacement, rendering the less noble Cu/CuAg regions sacrificial anodes. Control experiments established the essential roles of KCl and acetic acid in the formation of solid-hollow hybrid nanostructures (Figure S9). The quasi-spherical domains in both AuCu and AuAgCu JNSs underwent significant dissolution and structural collapse in the absence of either KCl or HAc. This confirms that both components are essential for achieving controlled synthesis and well-reserved porous architectures. Chloride ions stabilize the oxidized Cu/CuAg species as soluble chloro-complexes, facilitating their removal and modulating local reactivity, while oxygen acts as a co-oxidant to enhance and regulate the overall etching kinetics. Acetic acid fine-tunes this environment through its dual role as a pH buffer and a coordination modulator (via Ac^{-} anions), thereby preventing uncontrolled dissolution and promoting the development of spatially confined porosity. In addition, consistent with this mechanism, XRD analysis shows no detectable alloy phases, confirming that the resulting porosity arises from the controlled etching pathway mediated by $HAuCl_4$ and its synergistic auxiliaries, not from bulk alloy formation or interfacial intermixing.

3.4. LSPR Properties and Photothermal Conversion

The aqueous solution of Au NPs and AuCu-based hybrid nanostructures were investigated using UV-vis-NIR, revealing strong LSPR absorption in the NIR region for each product, indicating that they are all ideal photothermal conversion materials (Figure 5a). We further explored the NIR photothermal conversion performance of the five products using a laser and an infrared thermal imager, detecting their temperature changes under 808 nm laser irradiation. From the temperature rise and cooling curves of the five products, it was evident that all five products showed a significant temperature increase compared to the solvent water, with AuAgCu PHNSs showing the highest temperature increase, indicating that the products can effectively convert light energy into heat (Figure 5b). The thermographs also showed that the blank group did not change much in color after 20 min of 808 nm laser irradiation. In contrast, the thermographs of Au NPs, AuCu JNSs, AuCu PHNSs, AuAgCu JNSs, and AuAgCu PHNSs showed color changes from deep blue to orange-yellow to varying degrees (Figure 5c). The calculated ΔT values for Au NPs, AuCu JNSs, AuCu PHNSs, AuAgCu JNSs, and AuAgCu PHNSs were 27, 23.3, 27.8, 27.1, and 29.6 °C, respectively (Figure 5d). Additionally, the corresponding photothermal conversion efficiencies were calculated as

69.49%, 77.86%, 65.19%, 69.17%, and 67.15% (Figure S10, Table S3). Compared to the other four materials, AuAgCu PHNSs had stronger LSPR absorption at 808 nm, thus able to absorb more incident light, and its −ln(q) also showed a good linear relationship with time (Figure 5e). Since the photothermal conversion efficiency is influenced by multiple variables including ΔT_{max} and A_λ, its photothermal conversion efficiency is not necessarily the highest. Further, after performing five temperature rise-cooling cycles on AuAgCu PHNSs, the ΔT value did not decrease, indicating its excellent photothermal stability (Figure 5f).

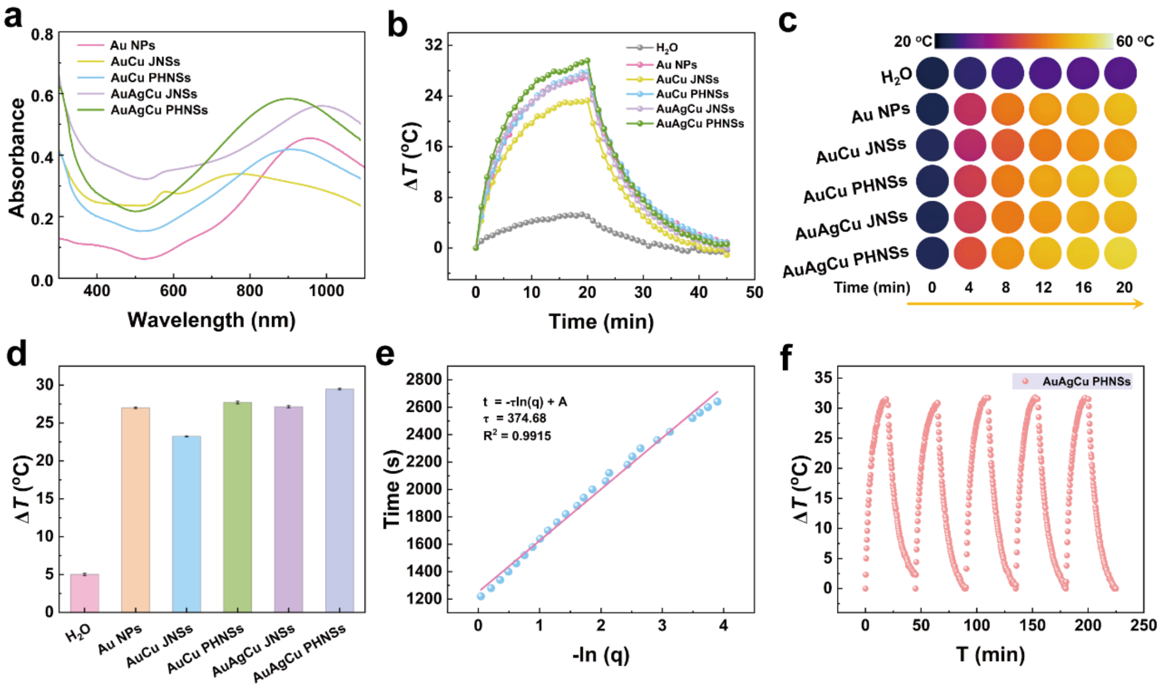

Figure 5. (**a**) UV-vis-NIR absorption spectra; (**b**) Temperature change (ΔT) over time during 20 min of 808 nm laser irradiation (1 W·cm^{-2}) followed by 25 min of cooling; (**c**) Infrared thermographic image under 808 nm laser irradiation; (**d**) Maximum temperature change (ΔT) after 20 min of irradiation; (**e**) Linear fitting of the cooling curve plotted as −ln(θ) versus time for AuAgCu PHNSs; (**f**) Photothermal stability of AuAgCu PHNSs assessed over five consecutive laser on/off cycles.

We further explored the photothermal performance of the five products in the NIR-II region. Under 20 min of 1064 nm laser irradiation, both the solvent water and the five products showed obvious temperature increase, with AuAgCu PHNSs showing the highest temperature increase (Figure 6a). The thermograph of the blank group changed from deep blue to red, while the thermographs of Au NPs, AuCu JNSs, AuCu PHNSs, AuAgCu JNSs, and AuAgCu PHNSs showed color changes from deep blue to orange-yellow (Figure 6b). The calculated ΔT values for Au NPs, AuCu JNSs, AuCu PHNSs, AuAgCu JNSs, and AuAgCu PHNSs were 25.9, 20.1, 24.6, 24.6, and 26.7 °C, respectively (Figure 6c), with corresponding photothermal conversion efficiencies of 32.11%, 30.40%, 31.72%, 31.64%, and 31.35% (Figure S11, Table S3). From Figure 6d, it can be seen that the −ln(q) of AuAgCu PHNSs still has a good linear relationship with time. However, unlike under 808 nm laser irradiation, AuAgCu JNSs has an absorption peak closer to the NIR-II region and has a higher absorbance. In addition, under 1064 nm laser irradiation, the photothermal stability of AuAgCu PHNSs was tested, and after five temperature rise-cooling cycles, it was found that the ΔT value of AuAgCu PHNSs did not change significantly in each cycle, indicating its excellent photothermal stability (Figure 6e). By comparing the results of recent studies on Au-based photothermal materials, the photothermal conversion efficiency of AuAgCu PHNSs is quite competitive (Table S4).

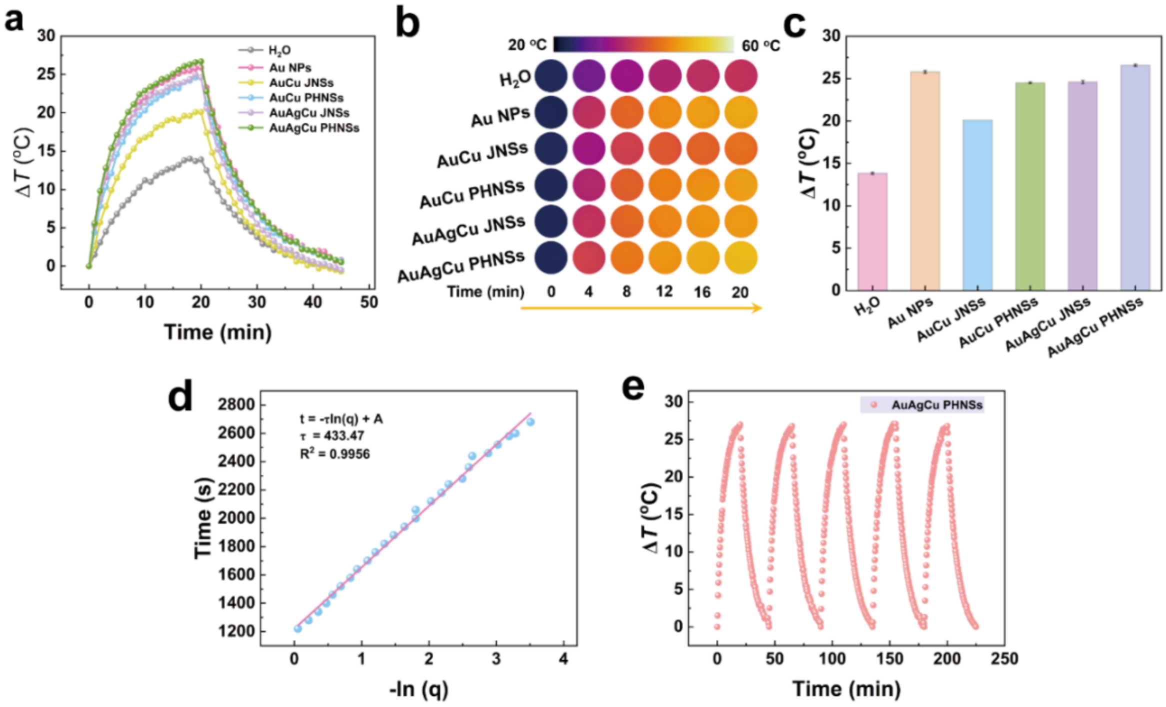

Figure 6. (**a**) Temperature change (ΔT) over time during 20 min of 1064 nm laser irradiation (1 W·cm^{-2}) followed by 25 min of cooling; (**b**) Infrared thermographic image under 1064 nm laser irradiation; (**c**) Maximum temperature change (ΔT) after 20 min of irradiation; (**d**) Linear fitting of the cooling curve plotted as –ln(θ) versus time for AuAgCu PHNSs; (**e**) Photothermal stability of AuAgCu PHNSs assessed over five consecutive laser on/off cycles.

3.5. *FDTD* Simulation

Figure S12 schematically illustrates the five numerical simulation models constructed to systematically investigate their near-infrared (NIR) photothermal properties. The models include Au nanoplate (Model Au NPs); a Cu nanosphere anchored with a Au nanoplate (Model AuCu JNSs); a Cu nanosphere anchored with a AuAg nanoplate (Model AuAgCu JNSs); and two porous hybrid nanostructures (Model AuCu PHNSs-I and AuCu PHNSs-II) composed of a Au nanosheet and a Cu nanosphere with pores of varying sizes. This series was designed to isolate the effects of material composition, heterojunction interfaces, and nanoscale porosity on plasmonic excitation and heat generation under NIR irradiation.

Due to the asymmetric structure, the absorption and scattering characteristics for multiple incident polarization directions were calculated and averaged, as shown in Figure 7. Figure 7a,c show that within the range of 300 to 1200 nm, Model Au NPs exhibit two absorption peaks under continuous illumination, but the absorption intensity is relatively low within the visible light range. For Model AuCu JNSs and Model AuAgCu JNSs, two small peaks can be observed within the range of 700 to 1050 nm, and a strong peak at 1100–1200 nm. The absorption peak of Model AuAgCu JNSs shifts slightly towards the blue compared to Model AuCu JNSs, which is attributed to the addition of Ag. Model AuCu PHNSs has three or more absorption peaks within the range of 300 to 1200 nm, and the absorption cross-section shows a significant increase. Particularly, the absorbance of Model AuCu PHNSs-II is relatively high in the range of 300–1200 nm. In Figure 7b,d, it can be observed that within the range of 600–900 nm, the scattering cross-section of Model AuCu PHNSs-II is significantly higher than that of other structures, which is unfavorable for its absorption performance. Considering the absorption and scattering effects throughout the entire range, Model AuCu PHNSs-I exhibits the strongest light harvesting capacity.

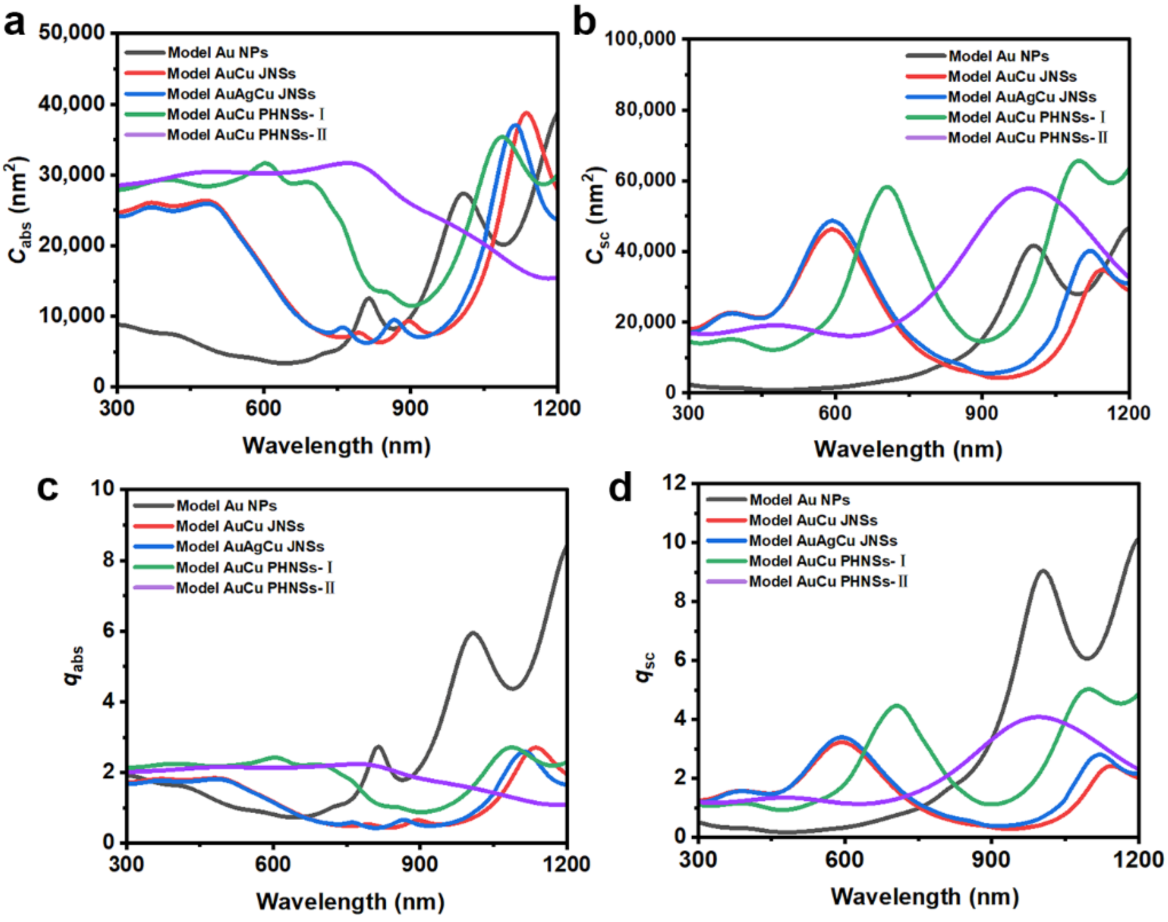

Figure 7. (**a**) absorption cross section; (**b**) scattering cross section; (**c**) absorption coefficient and (**d**) scattering coefficient of Model Au NPs, Model AuCu JNSs, Model AuAgCu JNSs, Model AuCu PHNSs-I, and Model AuCu PHNSs-II.

As shown in the electric and magnetic field energy distributions in Figure 8, a distinct electrical response appears at the edge of the Au NPs due to the concentration of electrons, resulting in local surface plasmon resonance (LSPR) [38]. In Model AuCu JNSs, the coupling effect between Au nanoplate and Cu nanosphere enhances the electromagnetic field. In contrast, for Model AuAgCu JNSs, when the Au nanoplate transforms into the AuAg nanoplate, the EM field distribution does not show any significant change. It is worth noting that in Model AuCu PHNSs-I and Model AuCu PHNSs-II, the cavity in the caged structure guides more electric fields into its interior, further enhancing the LSPR effect [39]. At the same time, the interaction between light and surface electrons increases, thereby improving light absorption capacity. Due to the smaller pores of Model AuCu PHNSs-II, the shortened path of light action, compared with Model AuCu PHNSs-I, the electric field is weaker.

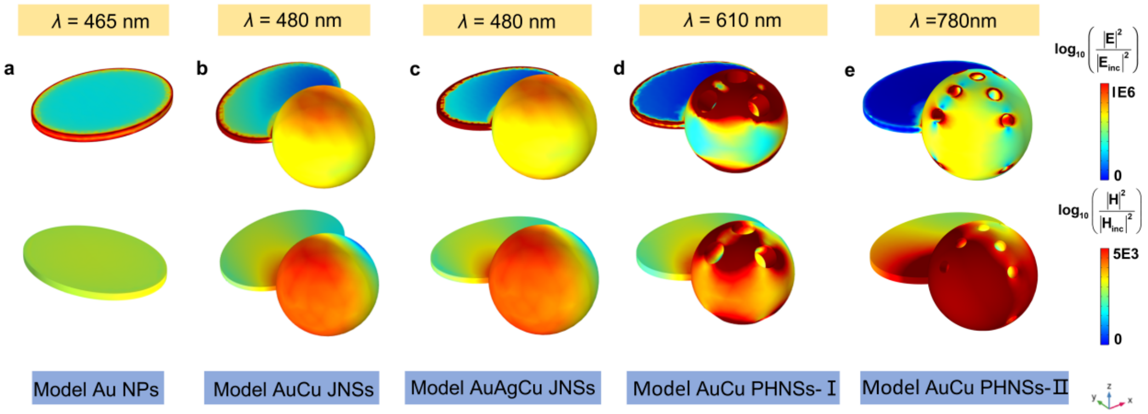

Figure 8. Electric field (top) and magnetic field (bottom) at the absorption peak in the x incident −z polarization direction for (**a**) Model Au NPs; (**b**) Model AuCu JNSs; (**c**) Model AuAgCu JNSs; (**d**) Model AuCu PHNSs-I and (**e**) Model AuCu PHNSs-II.

To visualize the photothermal response more clearly, we analyzed the two-dimensional temperature distributions (in x–y and z–y sections) of these models and the surrounding medium (Figure 9). Model AuCu PHNSs-I exhibited the greatest temperature rise of 44.1 K. In comparison, Models AuCu JNSs and AuAgCu JNSs showed increases of 32.8 K and 32.5 K, respectively. The temperature increase for Model AuCu PHNSs-II was more moderate at 8.5 K, due to its higher scattering efficiency. Model Au NPs showed only a minimal temperature rise of 5.4 K.

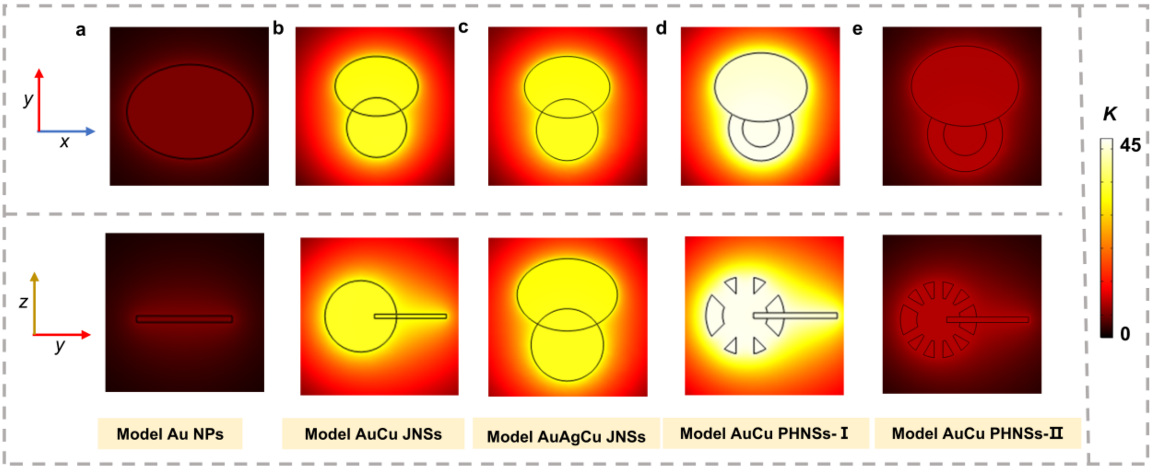

Figure 9. Temperature profiles of (**a**) Model Au NPs; (**b**) Model AuCu JNSs; (**c**) Model AuAgCu JNSs; (**d**) Model AuCu PHNSs-I and (**e**) Model AuCu PHNSs-II.

3.6. Photothermal Antibaceterial Test

The synthesized AuCu PHNSs and AuAgCu PHNSs represent promising NIR photothermal conversion agents capable of combating multidrug-resistant bacteria via photothermal therapy (PTT). The photothermal antimicrobial capability of these nanostructures was evaluated using the representative multidrug-resistant Gram-positive strain MRSA. Figure 10a demonstrates that even without NIR irradiation, both AuCu PHNSs and AuAgCu PHNSs exhibited significant antibacterial effects compared to the PBS control group. Notably, AuCu PHNSs showed superior intrinsic antibacterial activity, comparable to its performance under NIR irradiation. In contrast, AuAgCu PHNSs displayed markedly enhanced antibacterial efficacy only upon NIR irradiation for 10 min. Complete eradication of colonies (no growth) was observed for AuCu PHNSs diluted to 0.17×10^9 particles/mL, identifying this concentration as its MBC. These results indicate that the antimicrobial mechanism involves not only hyperthermia generated by the photothermal effect under NIR light but also significant growth inhibition mediated by the released Cu^{2+} ions at high concentrations. This synergistic effect is further corroborated by the data presented in Figure 10b,c. Given its optimal performance, AuCu PHNSs was selected for evaluating broad-spectrum antimicrobial efficacy. Testing againstrevealed that AuCu PHNSs, under NIR irradiation, effectively inhibited the growth of both Gram-positive and Gram-negative bacteria, achieving inhibition rates exceeding 99.9% in all cases (Figure 10d,e). Even in the absence of NIR irradiation, the AuCu PHNSs group exhibited substantially fewer bacterial colonies compared to the PBS group, with inhibition rates consistently above 60%. These findings further demonstrate that the potent antibacterial action of our material stems from the synergistic interplay between photothermal ablation and Cu^{2+} ion-mediated inhibition.

While the measured photothermal conversion efficiency of the AuCu-based hybrid nanostructures was comparable to that of pure Au nanoplates, the principal rationale for developing these complex architectures lies in their multimodal antibacterial action. In contrast to Au nanoplates, which function primarily as photothermal agents, the AuCu-based systems integrate photothermal therapy (PTT) with additional therapeutic mechanisms. Specifically, the porous, Cu-containing domains enable the sustained release of biocidal metal ions (e.g., Cu^{2+}, Ag^{+}), introducing a potent chemodynamic therapy (CDT) component. This synergistic PTT/CDT approach targets bacteria through concurrent physical and chemical pathways, which is anticipated to mitigate heat-shock resistance and lower the required laser irradiation dose for effective bacterial eradication.

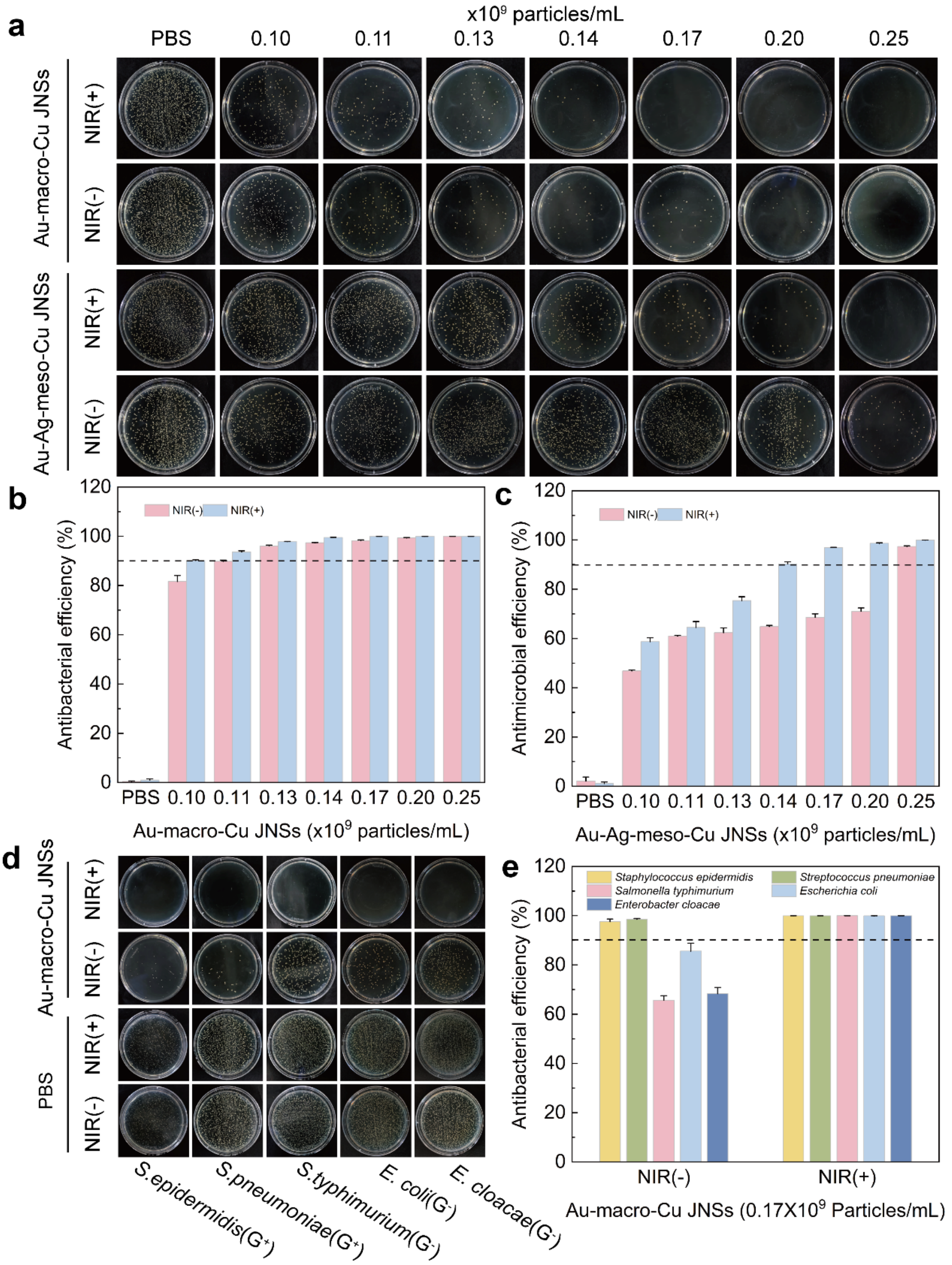

Figure 10. *In vitro* photothermal antibacterial performance of different materials. (**a**–**c**) Growth inhibition of MRSA on LB agar and antibacterial efficiency mediated by AuCu PHNSs and AuAgCu PHNSs treated with different concentrations, without or with NIR irradiation; (**d**,**e**) Broad-spectrum antimicrobial performance of AuCu PHNSs (0.17 × 10^9 particles/mL) without or with NIR irradiation.

4. Conclusions

In summary, we have developed a combined seeded growth and galvanic replacement strategy to synthesize AuCu-based solid–hollow hybrid nanostructures. The synthetic process—featuring unconformal deposition of quasi-spherical domains onto plate-like seeds, followed by spatially confined galvanic replacement moderated by KCl/acetic acid—yields porous hollow architectures integrated with solid Au plates. FDTD simulations confirm that the introduced porosity and structural asymmetry significantly enhance near-field plasmonic coupling and broadband absorption, particularly in the NIR region. These characteristics correlate with the observed high photothermal conversion efficiencies of 77.86% at 808 nm and 32.11% at 1064 nm, enabling effective eradication of multidrug-resistant bacteria under NIR irradiation. This work not only provides a versatile route to structurally tunable hybrid nanomaterials but also demonstrates, through both simulation and experiment, their promising potential as efficient photothermal agents for biomedical applications.

Supplementary Materials: The following supporting information can be downloaded at: https://media.sciltp.com/articles/others/2512301119183915/MI-25120148-Supplementary-Materials.pdf. Figure S1: TEM image of Au nanoplates (NPs). Figure S2: (**a**,**c**) SEM and (**b**,**d**) TEM images of (**a**,**b**) AuCu JNSs and (**c**,**d**) AuAgCu JNSs. Figure S3: EDX-STEM elemental maps of the AuCu JNS: (**a**) Overlay of Au (green) and Cu (red); (**b**) Cu map; (**c**) Au map. Figure S4: EDX-STEM elemental maps of the AuAgCu JNS: (**a**) Overlay of Au (green), Ag (blue), and Cu (red); (**b**) Cu map; (**c**) Ag map; (**d**) Au map. Figure S5: EDX-STEM line-scan profile: (**a**) AuAgCu PHNSs and (**b**) AuCu PHNSs. Figure S6: Histograms showing the pore size distribution of (**a**) AuAgCu PHNSs; (**b**) AuCu PHNSs. Figure S7: Histogram illustrating the atomic percentage of AuCu-based nanostructures as determined via EDS. Figure S8: Ag 3d XPS spectrum of AuAgCu PHNSs. Figure S9: TEM images of nanoparticles obtained using the same synthetic protocol as (**a**–**c**) AuCu PHNSs and (**d**–**f**) AuAgCu PHNSs, but with varied etching treatments: (**a**,**d**) $HAuCl_4$, (**b**,**e**) $HAuCl_4$ + KCl, and (**c**,**f**) $HAuCl_4$ + acetic acid. Figure S10: Determining the thermal transfer time constant (τ) of the system by plotting linear data from cooling times: (**a**) Au NPs; (**b**) AuCu JNSs; (**c**) AuCu PHNSs; (**d**) AuAgCu JNSs. Laser wavelength: 808 nm. Figure S11: Determining the thermal transfer time constant (τ) of the system by plotting linear data from cooling times: (**a**) Au NPs; (**b**) AuCu JNSs; (**c**) AuCu PHNSs; (**d**) AuAgCu JNSs. Laser wavelength: 1064 nm. Figure S12: The model schematics of (**a**) Model Au NPs; (**b**) Model AuCu JNSs; (**c**) Model AuAgCu JNSs; (**d**) Model AuCu PHNSs-I and (**e**) Model AuCu PHNSs-II. Table S1: XRD results of AuCu-based products in the current study. Table S2: Summary of the relative peak areas (%) for each split B.E. peak and the parameters used to fit the Cu 2p, Cu LMM, and Au 4f high-resolution XPS spectra. Table S3: Photothermal conversion efficiency of Au NPs, Au-Cu JNSs, Au-macro Cu JNSs, Au-Ag-Cu JNSs, and Au-Ag-meso Cu JNSs. Table S4: Comparative photothermal conversion performance of Au-based photothermal materials. References [40–47] are cited in supplementary materials.

Author Contributions: Q.Y.: conceptualization, methodology, investigation; Q.W.: software, validation, formal analysis, writing—original draft preparation; X.C.: data curation, visualization, writing—original draft preparation; X.S.: investigation, writing—original draft preparation; Y.W.: supervision, project administration, writing—reviewing and editing; X.W.: conceptualization, writing—reviewing and editing; Y.M.: resources, validation; P.Z.: methodology, supervision, writing—reviewing and editing; Y.Z.: conceptualization, supervision, funding acquisition, writing—reviewing and editing. All authors have read and agreed to the published version of the manuscript.

Funding: This work was financially supported by the Shandong Provincial Natural Science Foundation (grant No. ZR2025QC109 & ZR2022MB120), the Hundred Outstanding Talent Program of Jining University (grant No. 2020ZYRC05 & 2023ZYRC9), and the Science and Technology Innovation Team Foundation of Jining University (no. 23KCTD04 & 23KCTD05&24KCTD09). Additionally, support was provided by the Young Innovative Talents Introduction & Cultivation Program for Colleges and Universities of Shandong Province (granted by the Department of Education of Shandong Province, Sub-Title: Innovation Research Team on Organic Functional Molecules and Materials Design, No. 2023KJ277). This work is also supported by the University Feature Laboratory for Energy Conversion and Nanocatalysis of Shandong Province, the Suzhou Key Laboratory of Functional Nano & Soft Materials, the Collaborative Innovation Center of Suzhou Nano Science & Technology, the 111 Project, and the Joint International Research Laboratory of Carbon-Based Functional Materials and Devices.

Data Availability Statement: The data supporting this article have been included as part of the Supplementary Materials.

Conflicts of Interest: The authors declare no conflict of interest.

Use of AI and AI-Assisted Technologies: No AI tools were utilized for this paper.

References

1. Su, H.; Price, C.A.H.; Jing, L.; Tian, Q.; Liu, J.; Qian, K. Janus Particles: Design, Preparation, and Biomedical Applications. *Mater. Today Bio* **2019**, *4*, 100033. https://doi.org/10.1016/j.mtbio.2019.100033.
2. Wu, Z.; Li, L.; Liao, T.; Chen, X.; Jiang, W.; Luo, W.; Yang, J.; Sun, Z. Janus Nanoarchitectures: From Structural Design to Catalytic Applications. *Nano Today* **2018**, *22*, 62–82. https://doi.org/10.1016/j.nantod.2018.08.009.
3. Li, X.; Chen, L.; Cui, D.; Jiang, W.; Han, L.; Niu, N. Preparation and Application of Janus Nanoparticles: Recent Development and Prospects. *Coord. Chem. Rev.* **2022**, *454*, 214318. https://doi.org/10.1016/j.ccr.2021.214318.
4. Zhang, X.; Fu, Q.; Duan, H.; Song, J.; Yang, H. Janus Nanoparticles: From Fabrication to (Bio)Applications. *ACS Nano* **2021**, *15*, 6147–6191. https://doi.org/10.1021/acsnano.1c01146.
5. Li, Y.; Xia, M.; Zhou, J.; Hu, L.; Du, Y. Recent Advances in Gold Janus Nanomaterials: Preparation and Application. *Adv. Colloid Interface Sci.* **2024**, *334*, 103315. https://doi.org/10.1016/j.cis.2024.103315.
6. Li, C.-Y.; Duan, S.; Wen, B.-Y.; Li, S.-B.; Kathiresan, M.; Xie, L.-Q.; Chen, S.; Anema, J.R.; Mao, B.-W.; Luo, Y.; et al. Observation of Inhomogeneous Plasmonic Field Distribution in a Nanocavity. *Nat. Nanotech.* **2020**, *15*, 922–926. https://doi.org/10.1038/s41565-020-0753-y.
7. Wei, Y.; Qi, J.; Li, J.; Yu, C.; Zhao, J.; Pei, H. Precise Regulation of Surface Plasmonic Hotspots in an Au Split Nanoring Coupled System. *Results Phys.* **2024**, *61*, 107718. https://doi.org/10.1016/j.rinp.2024.107718.

8. Lu, Z.; Ji, J.; Ye, H.; Zhang, H.; Zhang, S.; Xu, H. Quantifying the Ultimate Limit of Plasmonic Near-Field Enhancement. *Nat. Commun.* **2024**, *15*, 8803. https://doi.org/10.1038/s41467-024-53210-8.
9. Zhang, D.; Chen, Y.; Hao, M.; Xia, Y. Putting Hybrid Nanomaterials to Work for Biomedical Applications. *Angew. Chem. Int. Ed.* **2024**, *63*, e202319567. https://doi.org/10.1002/anie.202319567.
10. Qiu, J.; Nguyen, Q.N.; Lyu, Z.; Wang, Q.; Xia, Y. Bimetallic Janus Nanocrystals: Syntheses and Applications. *Adv. Mater.* **2021**, *34*, 2102591. https://doi.org/10.1002/adma.202102591.
11. Li, Z.; Gong, J.; Lu, S.; Li, X.; Gu, X.; Xu, J.; Khan, J.U.; Jin, D.; Chen, X. Photothermal Lanthanide Nanomaterials: From Fundamentals to Theranostic Applications. *BMEMat* **2024**, *2*, e12088. https://doi.org/10.1002/bmm2.12088.
12. Zhang, M.; Ran, S.; Yin, X.; Zhang, J.; Sun, X.; Sun, W.; Zhu, Z. Mesoporous Polydopamine Nanoplatforms Loaded with Calcium Ascorbate for Amplified Oxidation and Photothermal Combination Cancer Therapy. *BMEMat* **2023**, *1*, e12041. https://doi.org/10.1002/bmm2.12041.
13. Chen, C.; Chu, G.; He, W.; Liu, Y.; Dai, K.; Valdez, J.; Moores, A.; Huang, P.; Wang, Z.; Jin, J.; et al. A Janus Au–Polymersome Heterostructure with Near-Field Enhancement Effect for Implant-Associated Infection Phototherapy. *Adv. Mater.* **2023**, *35*, 2207950. https://doi.org/10.1002/adma.202207950.
14. Xu, W.; Dong, C.; Hu, H.; Qian, X.; Chang, L.; Jiang, Q.; Yu, L.; Chen, Y.; Zhou, J. Engineering Janus Chemoreactive Nanosonosensitizers for Bilaterally Augmented Sonodynamic and Chemodynamic Cancer Nanotherapy. *Adv. Funct. Mater.* **2021**, *31*, 2103134. https://doi.org/10.1002/adfm.202103134.
15. Lv, Y.; Duan, S.; Wang, R. Structure Design, Controllable Synthesis, and Application of Metal-Semiconductor Heterostructure Nanoparticles. *Prog. Nat. Sci. Mater. Int.* **2020**, *30*, 1–12. https://doi.org/10.1016/j.pnsc.2019.12.005.
16. Zhao, T.; Chen, L.; Liu, M.; Lin, R.; Cai, W.; Hung, C.-T.; Wang, S.; Duan, L.; Zhang, F.; Elzatahry, A.; et al. Emulsion-Oriented Assembly for Janus Double-Spherical Mesoporous Nanoparticles as Biological Logic Gates. *Nat. Chem.* **2023**, *15*, 832–840. https://doi.org/10.1038/s41557-023-01183-4.
17. Yu, Y.; Lin, R.; Yu, H.; Liu, M.; Xing, E.; Wang, W.; Zhang, F.; Zhao, D.; Li, X. Versatile Synthesis of Metal-Compound Based Mesoporous Janus Nanoparticles. *Nat. Commun.* **2023**, *14*, 4249. https://doi.org/10.1038/s41467-023-40017-2.
18. Lv, K.; Hou, M.; Kou, Y.; Yu, H.; Liu, M.; Zhao, T.; Shen, J.; Huang, X.; Zhang, J.; Mady, M.F.; et al. Black Titania Janus Mesoporous Nanomotor for Enhanced Tumor Penetration and Near-Infrared Light-Triggered Photodynamic Therapy. *ACS Nano* **2024**, *18*, 13910–13923. https://doi.org/10.1021/acsnano.4c03652.
19. Peng, Z.; Huang, J.; Guo, Z. Anisotropic Janus Materials: From Micro-/Nanostructures to Applications. *Nanoscale* **2021**, *13*, 18839–18864. https://doi.org/10.1039/D1NR05499F.
20. Lu, Y.; Xu, R.; Liu, W.; Song, X.; Cai, W.; Fang, Y.; Xue, W.; Yu, S. Copper Peroxide Nanodot-Decorated Gold Nanostar/Silica Nanorod Janus Nanostructure with NIR-II Photothermal and Acid-Triggered Hydroxyl Radical Generation Properties for the Effective Treatment of Wound Infections. *J. Mater. Chem. B* **2024**, *12*, 5111–5127. https://doi.org/10.1039/D4TB00536H.
21. Li, S.; Zhu, J.; Shi, D.; Guo, P.; Wang, J.; Zhao, D.; Ma, Y. Interfacial Templating Strategy for Asymmetric Mesoporous Materials: Synthesis and Typical Applications. *Next Mater.* **2024**, *2*, 100144. https://doi.org/10.1016/j.nxmate.2024.100144.
22. Xia, X.; Xia, Y. Symmetry Breaking during Seeded Growth of Nanocrystals. *Nano Lett.* **2012**, *12*, 6038–6042. https://doi.org/10.1021/nl3040114.
23. Yang, T.-H.; Shi, Y.; Janssen, A.; Xia, Y. Surface Capping Agents and Their Roles in Shape-Controlled Synthesis of Colloidal Metal Nanocrystals. *Angew. Chem. Int. Ed.* **2020**, *59*, 15378–15401. https://doi.org/10.1002/anie.201911135.
24. Zeng, J.; Zheng, Y.; Rycenga, M.; Tao, J.; Li, Z.-Y.; Zhang, Q.; Zhu, Y.; Xia, Y. Controlling the Shapes of Silver Nanocrystals with Different Capping Agents. *J. Am. Chem. Soc.* **2010**, *132*, 8552–8553. https://doi.org/10.1021/ja103655f.
25. Xia, Y.; Gilroy, K.D.; Peng, H.-C.; Xia, X. Seed-Mediated Growth of Colloidal Metal Nanocrystals. *Angew. Chem. Int. Ed.* **2017**, *56*, 60–95. https://doi.org/10.1002/anie.201604731.
26. González-Rubio, G.; Mosquera, J.; Kumar, V.; Pedrazo-Tardajos, A.; Llombart, P.; Solís, D.M.; Lobato, I.; Noya, E.G.; Guerrero-Martínez, A.; Taboada, J.M.; et al. Micelle-Directed Chiral Seeded Growth on Anisotropic Gold Nanocrystals. *Science* **2020**, *368*, 1472–1477. https://doi.org/10.1126/science.aba0980.
27. Gao, C.; Goebl, J.; Yin, Y. Seeded Growth Route to Noble Metal Nanostructures. *J. Mater. Chem. C* **2013**, *1*, 3898–3909. https://doi.org/10.1039/C3TC30365A.
28. Xia, Y.; Xia, X.; Peng, H.-C. Shape-Controlled Synthesis of Colloidal Metal Nanocrystals: Thermodynamic versus Kinetic Products. *J. Am. Chem. Soc.* **2015**, *137*, 7947–7966. https://doi.org/10.1021/jacs.5b04641.
29. Zheng, Y.; Zeng, J.; Ruditskiy, A.; Liu, M.; Xia, Y. Oxidative Etching and Its Role in Manipulating the Nucleation and Growth of Noble-Metal Nanocrystals. *Chem. Mater.* **2014**, *26*, 22–33. https://doi.org/10.1021/cm402023g.
30. Liu, Y.-C.; Li, S.-Y.; Chen, X.-Y.; Chuang, Y.-C.; Wu, H.-L. Control of Oxidative Etching Rate of Cu Nanocubes in Synthesis of CuRu Nanocages and Nanoframes. *Chem. Mater.* **2023**, *35*, 136–143. https://doi.org/10.1021/acs.chemmater.2c02828.

31. Long, R.; Zhou, S.; Wiley, B.J.; Xiong, Y. Oxidative Etching for Controlled Synthesis of Metal Nanocrystals: Atomic Addition and Subtraction. *Chem. Soc. Rev.* **2014**, *43*, 6288–6310. https://doi.org/10.1039/C4CS00136B.
32. Makvandi, P.; Wang, C.-y.; Zare, E.N.; Borzacchiello, A.; Niu, L.-n.; Tay, F.R. Metal-Based Nanomaterials in Biomedical Applications: Antimicrobial Activity and Cytotoxicity Aspects. *Adv. Funct. Mater.* **2020**, *30*, 1910021. https://doi.org/10.1002/adfm.201910021.
33. Roper, D.K.; Ahn, W.; Hoepfner, M. Microscale Heat Transfer Transduced by Surface Plasmon Resonant Gold Nanoparticles. *J. Phys. Chem. C* **2007**, *111*, 3636–3641. https://doi.org/10.1021/jp064341w.
34. Rakić, A.D.; Djurišić, A.B.; Elazar, J.M.; Majewski, M.L. Optical Properties of Metallic Films for Vertical-Cavity Optoelectronic Devices. *Appl. Opt.* **1998**, *37*, 5271–5283. https://doi.org/10.1364/AO.37.005271.
35. Chen, X.; Qin, C.; Yang, L.; Li, X.; Wu, X.; Zhang, B. Triangular Pyramid Nanostructure Enhanced Photothermal Utilization of Noble Metal Nanoparticles. *Int. J. Therm. Sci.* **2024**, *200*, 108980. https://doi.org/10.1016/j.ijthermalsci.2024.108980.
36. Fu, X.; Tan, J.; Ma, Y.; Zhao, N.; Kong, Y.; Liu, F.; Zheng, Y.; Wang, Y.; Liu, M. *In Situ* Crumpling of Gold Nanosheets into Spherical Three-Dimensional Architecture: Probing the Aggregation-Induced Enhancement in Photothermal Properties. *Langmuir* **2022**, *38*, 1929–1936. https://doi.org/10.1021/acs.langmuir.1c03248.
37. Yang, Q.; Kong, H.; Tang, L.; Ma, Y.; Liu, F.; Liu, M.; Wang, Y.; Zhang, P.; Zheng, Y. Au–Cu Janus Nanostructures as NIR-II Photothermal Antibacterial Agents. *ACS Appl. Nano Mater.* **2024**, *7*, 20783–20792. https://doi.org/10.1021/acsanm.4c03673.
38. Zou, Y.; Qin, C.; Zhai, H.; Sun, C.; Zhang, B.; Wu, X. The Optical Characteristics of C@Cu Core-Shell Nanorods for Solar Thermal Applications. *Int. J. Therm. Sci.* **2022**, *182*, 107824. https://doi.org/10.1016/j.ijthermalsci.2022.107824.
39. Zou, Y.; Qin, C.; Yang, L.; Li, X.; Zhang, B.; Wu, X. Effect of Hollow Structure on Solar Thermal Applications of Au Nanodiscs. *J. Mol. Liquids* **2024**, *393*, 123528. https://doi.org/10.1016/j.molliq.2023.123528.
40. Jiang, T.; Song, J.; Zhang, W.; Wang, H.; Li, X.; Xia, R.; Zhu, L.; Xu, X. Au–Ag@Au Hollow Nanostructure with Enhanced Chemical Stability and Improved Photothermal Transduction Efficiency for Cancer Treatment. *ACS Appl. Mater. Interfaces* **2015**, *7*, 21985–21994. https://doi.org/10.1021/acsami.5b08305.
41. Bu, Y.; Huang, R.; Li, Z.; Zhang, P.; Zhang, L.; Yang, Y.; Liu, Z.; Guo, K.; Gao, F. Anisotropic Truncated Octahedral Au with Pt Deposition on Arris for Localized Surface Plasmon Resonance-Enhanced Photothermal and Photodynamic Therapy of Osteosarcoma. *ACS Appl. Mater. Interfaces* **2021**, *13*, 35328–35341. https://doi.org/10.1021/acsami.1c07181.
42. Song, Q.; Liu, Y.; Zhang, P.; Feng, W.; Shi, S.; Zhou, N.; Chu, X.; Shen, J. Au–Cu Bimetallic Nanostructures for Photothermal Antibacterial and Wound Healing Promotion. *ACS Appl. Nano Mater.* **2022**, *5*, 8621–8630. https://doi.org/10.1021/acsanm.2c02152.
43. Zhu, R.; Li, Y.; Zhang, X.; Bian, K.; Yang, M.; Cong, C.; Cheng, X.; Zhao, S.; Li, X.; Gao, D. Vapreotide-Mediated Hierarchical Mineralized Ag/Au Nanoshells for Photothermal Anti-Tumor Therapy. *Nanotechnology* **2019**, *30*, 055602. https://doi.org/10.1088/1361-6528/aaf0db.
44. Xu, M.; Lu, Q.; Song, Y.; Yang, L.; Ren, C.; Li, W.; Liu, P.; Wang, Y.; Zhu, Y.; Li, N. NIR-II Driven Plasmon-Enhanced Cascade Reaction for Tumor Microenvironment-Regulated Catalytic Therapy Based on Bio-Breakable Au–Ag nanozyme. *Nano Res.* **2020**, *13*, 2118–2129. https://doi.org/10.1007/s12274-020-2818-5.
45. Wang, Z.; Yu, N.; Li, X.; Yu, W.; Han, S.; Ren, X.; Yin, S.; Li, M.; Chen, Z. Galvanic Exchange-Induced Growth of Au Nanocrystals on CuS Nanoplates for Imaging Guided Photothermal Ablation of Tumors. *Chem. Eng. J.* **2020**, *381*, 122613. https://doi.org/10.1016/j.cej.2019.122613.
46. Sun, L.; Chen, Y.; Gong, F.; Dang, Q.; Xiang, G.; Cheng, L.; Liao, F.; Shao, M. Silicon Nanowires Decorated with Gold Nanoparticles via *in situ* Reduction for Photoacoustic Imaging-Guided Photothermal Cancer Therapy. *J. Mater. Chem. B* **2019**, *7*, 4393–4401. https://doi.org/10.1039/C9TB00147F.
47. Chen, M.M.; Hao, H.L.; Zhao, W.; Zhao, X.; Chen, H.Y.; Xu, J.J. A Plasmon-Enhanced Theranostic Nanoplatform for Synergistic Chemo-Phototherapy of Hypoxic Tumors in the NIR-II Window. *Chem. Sci.* **2021**, *12*, 10848–10854. https://doi.org/10.1039/d1sc01760h.